Optical phase stabilization for Raman-dressed potentials

K. Côté[1] and L. J. LeBlanc[1]

[1]*Department of Physics, University of Alberta, Edmonton AB, Canada*

The realization of spin-orbit coupled systems by way of laser-induced Raman transitions in ultracold atoms gives an invaluable approach to simulate quantum many body physics. In order to realize such phenomena in the lab, these systems must be coherent. We create a negative feedback phase stabilization interferometer in order to achieve coherence between two beams for use in spin-orbit coupling experiments. We utilize a 790nm Ti:Sapphire laser, acousto-optic modulators, and a Newport LB1005 proportional-integral servo controller. We test the stabilization under various conditions.

I. INTRODUCTION

Environments of ultracold atoms experiments are precisely engineered and parameters of the systems are known exactly. The unique nature of these types of experiments enable physics impossible in any other setting. A popular technique in ultracold atoms experiments involves using two or more laser beams to manipulate the potential energy landscape encountered by atoms via Raman transitions that change the atoms' internal atomic 'spin' [1]. Focused on the atoms, the two counter-propagating laser beams of slightly different energy allow us to establish these two-photon transitions between Zeeman energy levels. This leads to a phenomenon called *spin-orbit coupling* [2].

To obtain interesting potentials arising from spin-orbit coupling, the energy difference between the two beams must correspond to the energy difference between the states of interest, and in order to retain coherence in the quantum system the phase between the two beams must be well stabilized [1, 2]. In this paper we discuss a negative feedback phase stabilization interferometer system created in order to meet the latter demand and test the limits of the stability thereafter.

II. BACKGROUND

Some background is unavoidable in order to understand how our system will be utilized in future cold atoms experiments. In conventional systems, spin-orbit coupling is a relativistic effect in which an electrons' intrinsic angular momentum $\mathbf{L}$ due to its orbit around the nucleus is linked with its spin angular momentum $\mathbf{S}$ about its own axis. As an electron is a charged particle, these values are associated with magnetic moments $\boldsymbol{\mu_S} = -\mu_B g_s \mathbf{S}/\hbar$ and $\boldsymbol{\mu_L} = -\mu_B g_l \mathbf{L}/\hbar$, respectively, where μ_B is the Bohr magneton and g_s and g_l are called *g-factors* [4]. The effect is most easily understood in terms of the interaction between an electron's spin magnetic moment $\boldsymbol{\mu_S}$ and the external magnetic field created by the orbiting nucleus (in the electrons frame of reference). Electrodynamics tells us a rotating, electrically charged body creates a magnetic dipole, meaning the electron acts like a tiny

bar magnet with associated magnetic moment $\boldsymbol{\mu_S}$ about its own axis. If we consider a frame in which the electron is stationary, the electron will see the nucleus of the atom orbiting about it. The orbiting nucleus creates an external magnetic field which exerts a torque on $\boldsymbol{\mu_S}$, acting to align it with the field. The Hamiltonian for this interaction is $H = -\boldsymbol{\mu_S} \cdot \mathbf{B}$, with $\mathbf{B}$ being the magnetic field of the nucleus. It is easy to show that this magnetic field is proportional to $\mathbf{L}$ as $\mathbf{B} \sim -\mathbf{v} \times \mathbf{E} \sim \mathbf{r} \times \mathbf{v} \sim \mathbf{r} \times \mathbf{p} \sim \mathbf{L}$. The interaction energy, then, depends on the relative orientation of $\boldsymbol{\mu_S}$ and $\boldsymbol{\mu_L}$ with respect to one another. Accounting for the electron's stationary frame being non-inertial, we arrive at the total spin-orbit interaction [4]:

$$H_{SO} = \frac{1}{2} \left(\frac{Ze^2}{4\pi\epsilon_0} \right) \left(\frac{g_s}{2m_e^2 c^2} \right) \frac{\mathbf{L} \cdot \mathbf{S}}{r^3},$$

where Z is the total charge in the nucleus. Because of the momentum dependent interaction energy, the alignment of $\boldsymbol{\mu_S}$ depends on the electron's velocity as $\mathbf{p} = m_e \mathbf{v}$. This is a symmetry-breaker; in the presence of spin-orbit coupling, the Hamiltonian no longer commutes with $\mathbf{L}$ or $\mathbf{S}$. This in turn creates a splitting of the energy levels of the atom — along with a relativistic correction this amounts to what is called *fine structure* splitting.
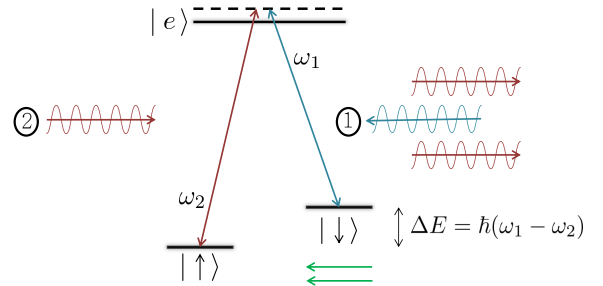

FIG. 1: Two-photon Raman process between Zeeman states labeled "spin-up" $|\uparrow\rangle$ and "spin-down" $|\downarrow\rangle$. The figure depicts the process corresponding to absorption of ω_1 from the right, first, but also happens in reverse order from the left. The two green arrows represent momentum kicks from processes ① and ② of magnitude $\hbar\omega_1/c$ and $\hbar\omega_2/c$, respectively.

In order to achieve this phenomenon in the laboratory we utilize Raman transitions between states using two

counter-propagating laser beams whose frequencies, ω_1 and ω_2, are set to resonate with the transition from one energy level to the other. We're able to *create* these energy levels by applying an external magnetic field to the atoms. Applying this magnetic field to the atoms adds another term to the Hamiltonian, $H_Z = -\boldsymbol{\mu} \cdot \mathbf{B}$, where $\boldsymbol{\mu} = \boldsymbol{\mu_S} + \boldsymbol{\mu_L}$ and $\mathbf{B}$ is the external magnetic field [3]. This splitting of hyperfine energy states is called the Zeeman effect, named after the Dutch physicist Pieter Zeeman. The energy difference between two Zeeman states with an applied magnetic field is given by

$$\Delta E = g_F m_F \mu_B B,$$

where g_F is called the Landé g-factor[1] and m_F is a quantum number describing the total angular momentum [4]. We're able to set ΔE by choosing an appropriate magnetic field; we want to make ΔE large enough that we can distinguish between the two states, but small enough that the corresponding magnetic field can be easily created in the lab. For example, using $g_F = 1/2$ for the ^{87}Rb atoms commonly used in the lab, $m_F = 1$, and a 5 G ~ 0.0005 T magnetic field, the energy between Zeeman states is $\Delta E \simeq 2.3 \times 10^{-27}$ J. This implies the frequency separation of our beams for this scenario should be $\delta\omega/2\pi = (\omega_1 - \omega_2)/2\pi = \Delta E/\hbar \simeq 3.5$ MHz. Once we match the beams to this energy difference specified by a reasonably attainable magnetic field we get resonant Raman transitions. The resonance involves the atom continuously absorbing photons from one beam and emitting them into the other. If we follow the process portrayed in fig. 1, the atom first absorbs a photon from ω_1 with just the right frequency and is therefore excited. Because the energy of the absorbed photon corresponds to the transition from the "$|\uparrow\rangle$" state, this state receives a momentum kick to the left. The beam propagating from the left, ω_2, de-excites the atom to the other Zeeman level emitting two identical photons of the same frequency to the right by way of stimulated emission. The $|\uparrow\rangle$ state receives another momentum kick to the left. The same process happens in reverse to the $|\downarrow\rangle$ state: absorption from ω_2 and stimulated emission into ω_1 result in momentum kicks to the right. The Raman transitions couple spin states of the atoms but as they are moving the Doppler effect works to detune the beams away from resonance, creating velocity dependence in the coupling mechanism. In other words these transitions provide the velocity-dependent link we need in order to couple the spin and momentum of the atom.

III. METHODOLOGY

What we've learned so far: to achieve spin-orbit coupling in the lab we need two phase-stabilized beams of slightly different frequency. When we talk about electromagnetic radiation we think of a signal of the form $A\sin(\omega t + \phi)$ where A is the amplitude, ω is the frequency, and ϕ is the phase. The phase, or phase *shift*, measures an angular displacement relative to another signal (say $A\sin(\omega t)$). Since the phase is defined relatively we cannot necessarily measure the phase of each beam directly. To measure the phase shift between our beams we created an interferometer detailed in fig. 2. We can extract information about the phase difference between two beams by superimposing them — beams that arrive in phase will constructively interfere and beams arriving out of phase will interfere destructively. Using this principle we can track changes in the phase difference.

Once we were able to track how the phase difference $\delta\phi$ changes over time we want to stabilize it, or, set $\delta\phi = 0$. To do this we created a negative feedback routine that works to automatically suppress deviations in $\delta\phi$ from zero.

A. Interferometer

Starting with a single emission from a tuneable 2W Ti:Sapphire laser set to emit at 790nm[2], the light first travels through a $1/2$ waveplate. Throughout the system the $1/2$ waveplates are used for polarization control. A linearly polarized beam travelling through the waveplate will rotate the polarization vector through 2θ, where θ is defined as the angle between the polarization vector and the fast axis of the waveplate. They essentially mirror the light's polarization in the fast axis. The beam then travels through a polarizing beam splitter (PBS) used as a power control; only half of the beams original power is transmitted and the other half is reflected away and dumped. The beam is then split once again using a PBS cube into the two beams we need.

We know from section II the beam's must have a frequency difference that corresponds to the energy difference ΔE between the two Zeeman states. We accomplish this by using acousto-optic modulators (AOMs). AOMs take advantage of the acousto-optic effect to diffract the laser beam using sound waves. The effect involves a change in the index of refraction due to a mechanical strain. The acoustic waves inside the AOM's interior crystal created by some radio frequency (RF) source are pressure waves, whose crests and troughs consist of compressions and expansions that periodically modulate the index of refraction of the crystal. In simple terms the sound waves create a diffraction grating in

---

[1] The Landé g-factor incorporates g_l, g_s, and g_I which characterizes the magnetic moment of the nucleus

---

[2] 790nm corresponds to a transition between hyperfine states in ^{87}Rb atoms
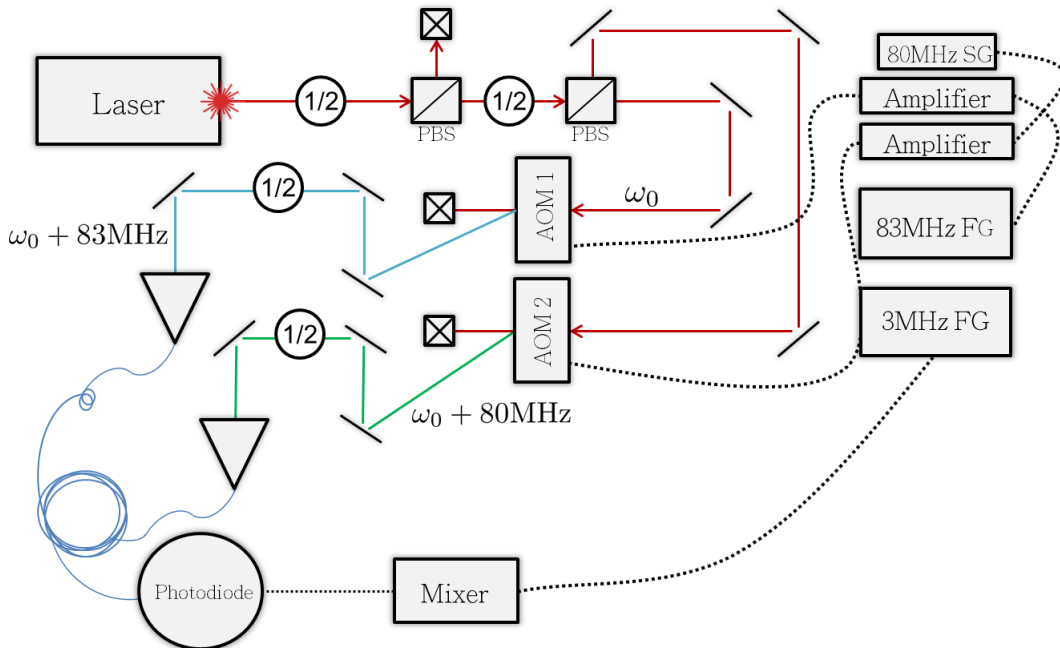
FIG. 2: Schematic diagram of the interferometer. The symbol ⊠ represents a beam dump. The colored lines represent the beams at different frequencies – the red beam ($\omega_0/2\pi$) corresponds to 790nm or 380THz, the blue beam ($\omega_0/2\pi + 83$ MHz) to 380 THz + 83 MHz, and the green beam ($\omega_0/2\pi + 80$ MHz) to 380 THz + 80 MHz.

the crystal. The AOMs shift the frequency of the light according to $\omega'/2\pi \rightarrow \omega/2\pi + mF$, where ω is the frequency of the original beam, m is the order of the diffracted beam, and F is the frequency of the sound wave. Both beams are shifted separately using two different RF sources and two separate AOMs. It is at this point that we are introducing a relative frequency shift between beams.

We use two RF sources: an 83 MHz function generator supplies one of the AOMs and a signal generator set at 80 MHz supplies the other. The first order ($m = 1$) diffracted beam is allowed to continue while the zeroth order beam with the same original frequency ω_0 is dumped. The two beams now have frequencies $\omega_1/2\pi = \omega_0/2\pi + 83$ MHz $\sim$ 380 THz + 83 MHz and $\omega_2/2\pi = \omega_0/2\pi + 80$ MHz $\sim$ 380 THz + 80 MHz, meaning the difference in frequencies $\delta\omega/2\pi = 3$ MHz. This value should correspond to the energy difference between the Zeeman states created by an appropriate external magnetic field. Both beams are then coupled into a polarization-maintaining fiber that couples both beams into a single mode output. Our coupling strength for each beam-to-fibre transition was just under 60%. As discussed later in section VII A this setup granted us a higher quality signal at the photodiode compared with earlier iterations. The fiber works to align the two beams precisely onto the photodiode, in turn converting light
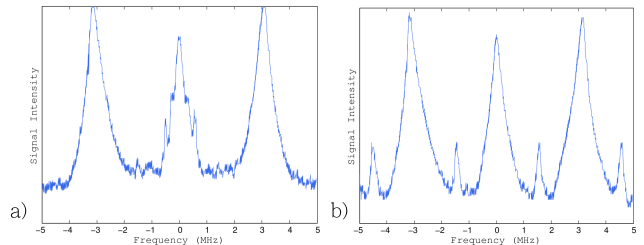

FIG. 3: Logarithmic signal intensity versus frequency — a) signal measured at the photodiode, b) signal created by the 3 MHz function generator.

into current. The beat note reaching the photodiode in this configuration is shown in fig. 3 a[3].

An inquisitive reader will ask why we use one AOM on each beam and not a single AOM on only one of the beams: we want ω_1 and ω_2 to be close in value and we require the ability to change the frequency of one with respect to the other via modulation of the RF input. This is discussed in the next subsection.

————

[3] see section VII B for information about how we obtained these plots

B.   Phase Stabilization

We can follow the beam as it enters the photodiode. Each separate signal can be represented by $A_1 \sin(\omega_1 t + \phi_1)$ and $A_2 \sin(\omega_2 t + \phi_2)$, but once overlapped in the optical fiber, the signals are multiplied,

$$V_1 = A_1 A_2 \sin(\omega_1 t + \phi_1)\sin(\omega_2 t + \phi_2)$$
$$= \frac{1}{2}A_1 A_2[\cos(\delta\omega t + \delta\phi) - \cos((\omega_1 + \omega_2)t + (\phi_1 + \phi_2))],$$

where we have defined the phase difference $\delta\phi = \phi_1 - \phi_2$, and $\delta\omega = \omega_1 - \omega_2$.

At multiple stages we filter out the higher frequency components in order to isolate $\delta\phi$. Connected to the photodiode output, the first low-pass filter (LPF) at 48MHz filters out the huge $\omega_1 + \omega_2$ signal:

$$V_2 = \frac{1}{2}A_1 A_2 \cos(\delta\omega t + \delta\phi).$$

By inspection – and by recalling trigonometry rules – we can see that in order to isolate $\delta\phi$ further, we could multiply this signal by another signal of the same frequency. This would get rid of the frequency dependence in one term. A function generator supplies a reference signal $\cos(\delta\omega t + \phi_{REF})$ with the same 3 MHz frequency as shown in 3 b. Now that we have introduced our three signal generators, it is important to make a note about the phase between all of these devices. In order to assure coherency of the system, the devices should be synchronized. If there is some random phase slips between them that make these devices incoherent, the frequency they each provide to the system would have a random phase and the final signal I'm about to describe wouldn't necessarily be resolved. To combat this, we incorporate a linkage between the generators by way of a 10 MHz timebase. A 10 MHz signal from the function generator set at 3 MHz connects to the 83 MHz function generator through a BNC input explicitly called "Timebase IN". On the same device we connect the "Timebase OUT" to the 80 MHz signal generator. This works to keep these three devices harmonized and is absolutely imperative. Once the timebase connection is implemented we use a mixer to multiply the filtered photodiode signal (V_2) with the $\cos(\delta\omega t + \phi_{REF})$ reference signal:

$$V_3 = \frac{1}{2}A_1 A_2 \cos(\delta\omega t + \delta\phi)\cos(\delta\omega t + \phi_{REF})$$
$$= \frac{1}{4}A_1 A_2[\cos(\delta\phi - \phi_{REF}) + \cos(2\delta\omega t + (\delta\phi + \phi_{REF}))].$$

This mixed signal should have distinct peaks at $2\delta\omega = 6$ MHz. Our mixer output signal is shown in fig 4.
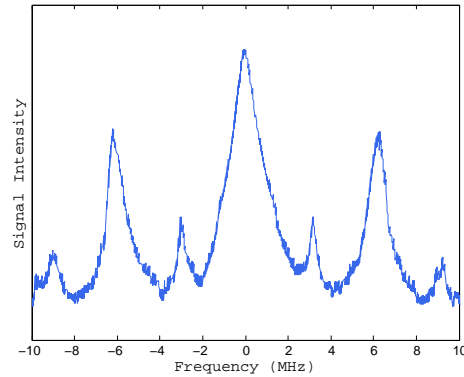

FIG. 4: Logarithmic signal intensity versus frequency of the mixed signal.

Another LPF at 1.6 MHz is used to filter out the larger signal, arriving at $V_{final} \sim \cos(\delta\phi - \phi_{REF})$. We connected an oscilloscope to the output of the mixer so we could measure the response of varying ϕ_{REF}. Fig 5 shows five sample signals attained during a 1000 Hz ramp variation of ϕ_{REF} from $-180°$ to $180°$. The plot shows variations on the order of 0.2V which is more than enough to be able to track changes in $\delta\phi$. If we stick with $\phi_{REF} = \pi/2$, $V_{final} \sim \cos(\delta\phi - \pi/2) \propto \sin(\delta\phi)$ and we can measure the phase difference directly.
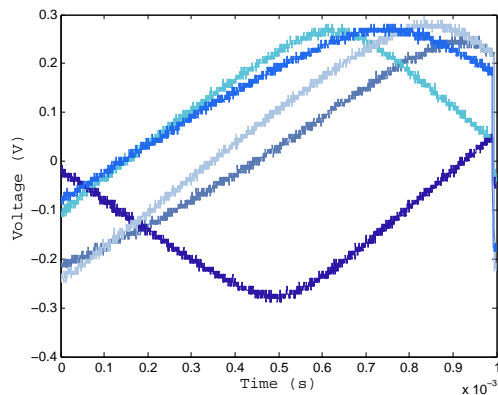

FIG. 5: Sample signals measured as a response to varying the reference phase ϕ_{ref} of the 3 MHz function generator. We varied ϕ_{ref} using a 1000 Hz ramp signal, allowing ϕ_{ref} to vary from $-180°$ to $180°$ in 0.001 s. The samples appear so different becaue the initial phase is random due to phase variations in the unstabilized system.

In order to control the phase difference we make use of a Newport LB1005 *proportional-integral* (PI) servo controller. Generally, a PI controller continually calculates an error value equal to the difference between a measured "process" variable ($\delta\phi$) and its desired reference point ($\delta\phi = 0$). The filtered signal from the mixer with $\phi_{REF} = \pi/2$ is fed into the controller as the process signal, and a 50Ω resistor is placed on the reference input. The controller subtracts the voltage
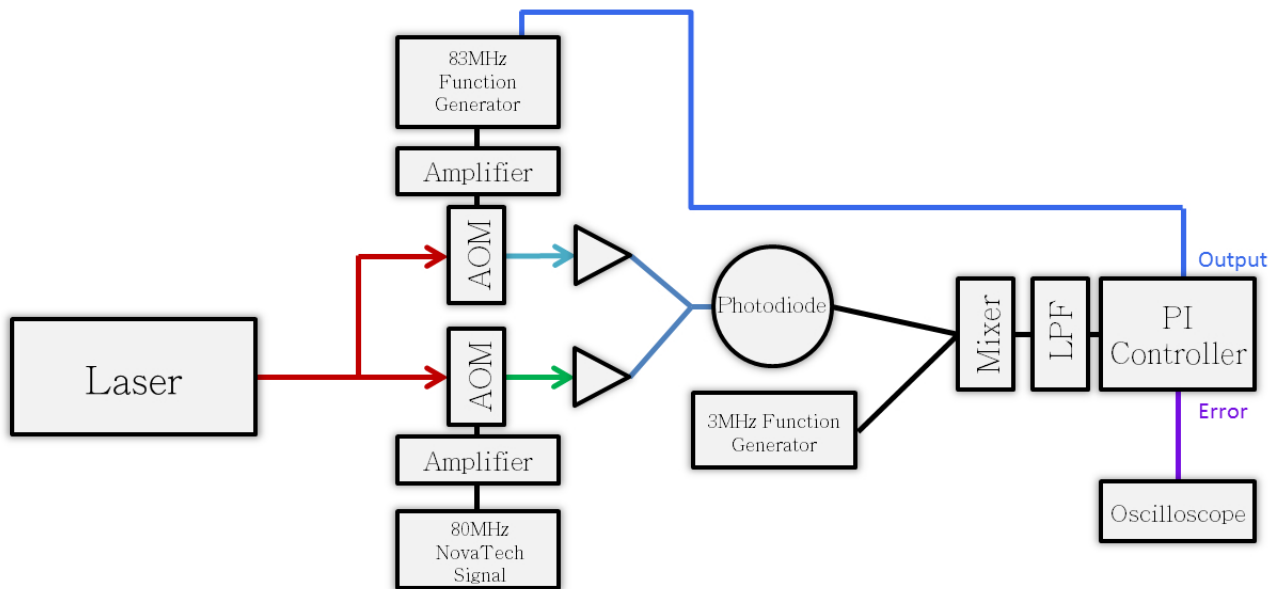
FIG. 6: The stabilization loop.

from these two inputs to generate an *error* signal. An error output on the front of the controller allows us to monitor this voltage using an oscilloscope. The control *output* supplies the regulator signal from the PI filter. This output is connected as an external frequency modulation to the 83 MHz function generator that in turn controls an AOM. This effectively completes the stabilization loop as summarized in fig 6. When the function generator detects this modulation, it will change its frequency F accordingly. Recall from section III A that the beam gets diffracted at the AOM according to $\omega'/2\pi = \omega_0/2\pi + mF$ so changing F in turn changes the beams' frequency. This process happens until the perturbation in the error signal is quenched and $\delta\phi = 0$.

As named, the PI controller has two types of feedback mechanisms. The proportional control produces an output that is proportional to the error, while the integral control produces output proportional to the magnitude and duration of the error. The controller allows you to pick the "amount" of each mechanism used to minimize the error. For our purposes we found that using strictly the proportional setting was enough to incite a quick (almost instant) correction. Subsequently, the low-frequency gain limit that controls the amount of integral correction (LF Gain Limit) was set to "Prop" deeming the "PI Corner" setting, which chooses at what frequency the controller switches between the two mechanisms, redundant. This is further discussed in section V.

It might now be valuable to concretely establish why changing the frequency of one of the beams effects the phase. Say we have two signals that are initially synchronized in phase but have a different frequency: $S_1 =$

$A_1 \sin(\omega_1 t)$ and $S_2 = A_2 \sin(\omega_2 t)$. After a time Δt the signals will develop a differential total phase shift $\Delta\phi = \Delta\omega \times \Delta t$. We can think of the phase shift being built up over time by the frequency difference. We can also think about the units of measurement: $[(\Delta\omega)(t)]=[(\text{cycles s}^{-1})(\text{s})]=$ number of cycles. So, for example, two signals differing in frequency by 100 Hz get progressively out of phase with each other by 100 cycles every second. This justifies the use of frequency modulation to change the phase.

IV. RESULTS

We're able to measure the amount by which the error in $\delta\phi$ is reduced when the loop is completed. Looking at fig 7 we immediately see the reduction in error. We quantify this by a *reduction factor*, σ. Described by the following formula, it is simply the peak-to-peak width of the unstabilized signal divided by the same value of the stabilized one:

$$\sigma = \frac{\text{height while not stabilized}}{\text{height while stabilized}},$$
$$= \frac{0.078 \text{ mV} - (-0.08 \text{ mV})}{|-0.076 \text{ mV}| - |-0.074 \text{ mV}|},$$
$$= \frac{0.158}{0.002} = 79 \pm 1.$$

This signifies the ratio by which the error is reduced. In calculating the uncertainty we assumed the error in both measurements was the resoloution acheiveable by the oscilloscope, 0.002 mV, and used the propagation
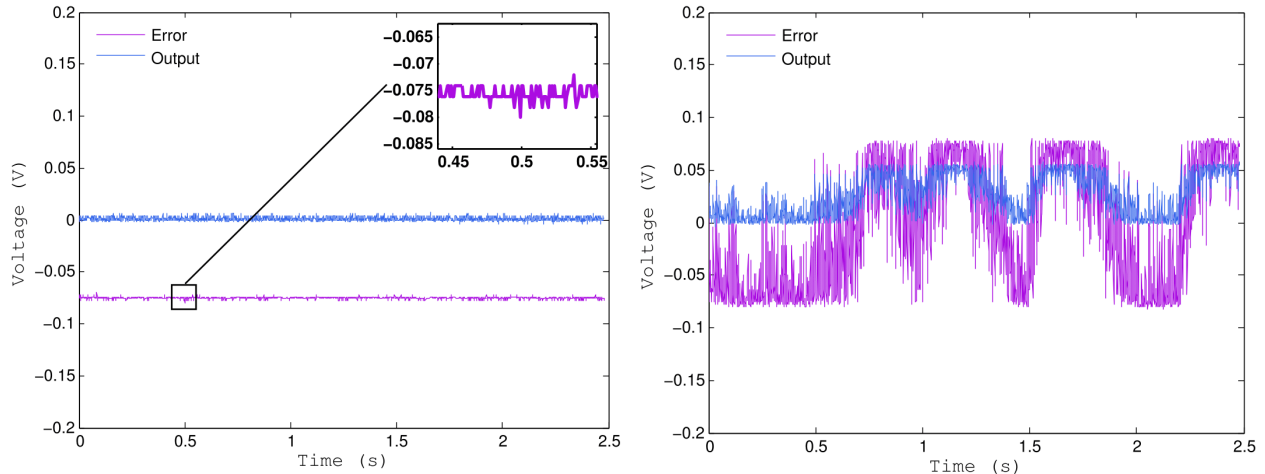
FIG. 7: Comparison of controller output and error signals for stabilization on (left) and off (right).

of uncertatainties for quotients $\sqrt{\left(\frac{\delta a}{a}\right)^2 + \left(\frac{\delta b}{b}\right)^2}$. This gives us a rough estimate. We can consider this system well stabilized, but there are certain places where we can further optimize the stabilization routine and increasing the fiber coupling alignment is a large part of this. Perfecting the alignment will increase the signal strength at each step and will improve the error signal at the final stage.

It would be beneficial to know by which amount the frequency changes when we see large error signals. As a test we hooked up a constant another signal generator directly to the controller along with the 50Ω resistor. We varied the voltage and observed the resulting frequency shifts of the 83 MHz function generator on the spectrum analyzer. Using this method, and considering our controller was set to have a "Modulation Deviation" of 1 MHz, we reasoned that a 1 V error signal corresponded to a 1 MHz shift in the frequency. If we consider that the controller has two different mechanisms that both depend on time in a different way, we can say that the frequency response for some time t, $\Delta\omega_1 t$ goes like $\Delta(\delta\phi)$. For example, take $t = 1$ and say the error voltage is measured is around 20 mV, then the change $\Delta\omega_1 \sim \frac{1\ \text{MHz}}{1\ \text{V}} 20\ \text{mV} \sim 20$ kHz. The system can deliver either a large frequency response over a short time period or a smaller frequency change over a longer time period. We will show in the next section that for our setup, the former tends to occur.

V. TESTING STABILITY

It was necessary to determine how the system would react to different mechanical, structural, and other disturbances. In the following discussion recall that the error signal from the controller is the difference between our signal, $\sin(\delta\phi)$, and the reference (0V). The controller will output a signal hoping to extinguish the error.
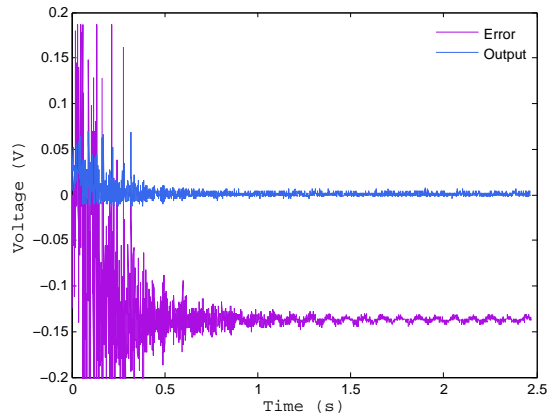

FIG. 8: The response measured from the system during a hit. The purple (lower) line represents the error signal measured at the controller [see fig 6] while the blue (upper) line shows the controllers output signal.

Fig. 8 shows the system's response to a hit on the table where it lays. We see that the system returns to a stable point nearing the end of the time scale depicted on the plot and there is not a large output response needed to correct the perturbation. Fig. 9 shows the evolution of the frequency spectrum with time. Focusing on the spectrum at $t = t_3$ (the time of the hit), we see that although the peak of the spectrum doesn't shift from 83 MHz we do notice the appearence of large sidebands. A small amount of frequency "shift" is needed to correct the phase.

Fig. 10 shows a reaction as heat is imparted on the system. We used a heat gun to carefully create an encompassing "heat bath". Admittedly, this was not the most
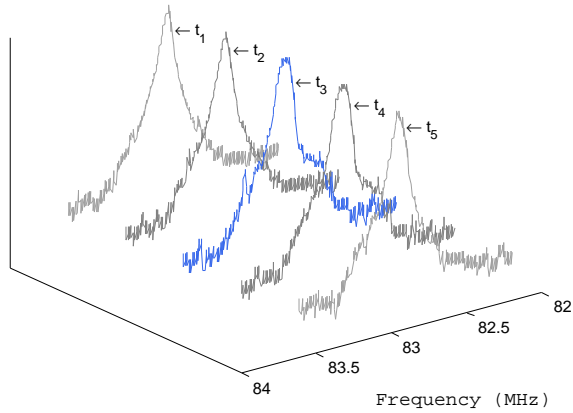
FIG. 9: Evolution of the frequency spectrum of the 83 MHz function generator from some earlier time t_1, to the time of the hit, t_3, followed by some later times.

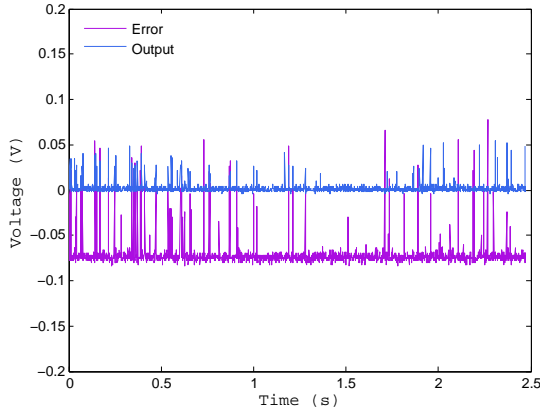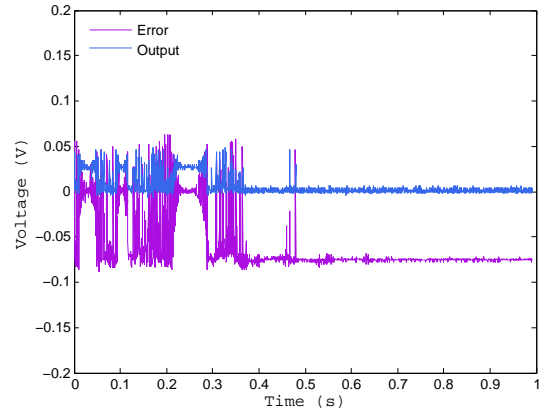FIG. 11: The response of the system from rapid movement of the coupling fiber. The purple (lower) line represents the error signal measured at the controller while the blue (upper) line shows the controllers' output signal.

FIG. 10: The purple (lower) line represents the error signal measured at the controller while the blue (upper) line shows the controllers output signal. Heat added to the system creates rapid spikes that are immediately quenched.
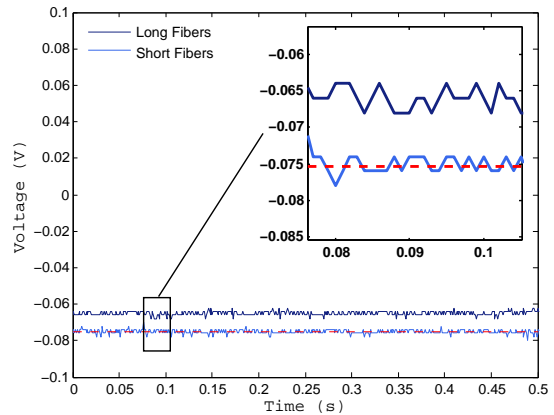

FIG. 12: Comparing the stabilization precision for long (upper line) and short (lower line) fibers. In order to show both on the same plot we have offset the signal corresponding to the long fiber 0.01V. The dashed red line shows the real, measured position.

precise method of testing for heat sensitivity because we were not able to measure the ambient temperature, and not all components were the same temperature at the same time. You can see in the figure the response to heat but no indication of a cooling period. Instead there are sporadic jumps where certain parts of the system were slightly warmer than others. In order to legitimately test heat sensitivity the interferometer should be placed in a thermal chamber, heated comprehensively, and then allowed to cool. It is advantageous to verify this sensitivity as temperature plays an important role in the index of refraction of the air which could affect the stability of the system.

Fig. 11 depicts the system's response during rapid movement of the coupling fiber. The fiber attached to the photodiode was shaken. We can see that there is a

large response but no lasting effect on the stabilization. Although the system reacts quickly to these wiggles, it seems favourable to secure the fibers to the table or some other surface so they are not in a position to affect the stabilization negatively. Along the same lines, we saw it necessary to see if there would be any reduction in stabilization precision if we switched out the short 30cm fibers for much longer ones. These longer fibers would be required when integrating the interferometer into a much larger system in order to perform spin-orbit coupling. Fig. 12 shows the comparison of error signals with the long and short fibers. The peak-to-peak height of the error signal is a measurement of the precision we are able to achieve. Looking at the magnified section we see both
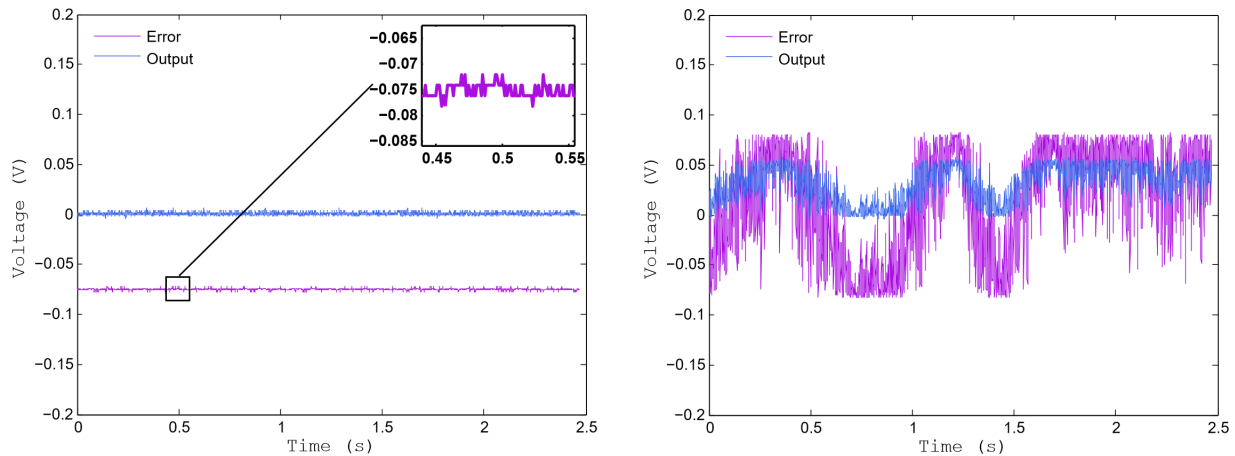
FIG. 13: Comparison of controller output and error signals for stabilization on (left) and off (right) using long fibers.

lines have a height on the order of a few millivolts; more precisely, averaging over the magnified window, the long fibres measure 0.003 mV and the short fibers measure 0.002 mV. Fig. 13 shows the signals when the feedback loop is turned on and off, respectively. As before we can measure the peak-to-peak height of the error signal to determine the proportional reduction in the error:

$$
\begin{aligned}
\sigma &= \frac{\text{height while not stabilized}}{\text{height while stabilized}}, \\
&= \frac{0.081 \text{ mV} - (-0.08 \text{ mV})}{|-0.077 \text{ mV}| - |-0.074 \text{ mV}|}, \\
&= \frac{0.161}{0.003} = 53.\overline{6} \pm 0.7,
\end{aligned}
$$

where we estimated the error in the same way as before. The stabilization routine minimizes the drift in the phase shift $\delta\phi$ by a factor of 54. When we performed this calculation before using our original fibers we calculated the minimization factor to be 79. These factors are relatively close in magnitude, and $\sigma_{longfiber} = 54$ is still large enough to consider the system well stabilized, and the long fibers would be adequate to use in further experiments.

VI. CONCLUSION

We have contructed an interferometer incorporating a succesful phase stabilization routine for use in future quantum, ultracold gas experiments. The interferometer consists of two beams frequency shifted by acousto-optic modulators with radio frequency (RF) sources resulting in a frequency spread of 3 MHz. We use a Newport LB1005 proportional-integral controller connected to one RF sources to vary the frequency of one beam. This works to minimize the phase shift between the two beams continually. We noted that establishing a time-base between generators supplying signals throughout

the system is imperative.

We tested the stabilization under different conditions and found the system to be extremely responsive — in most case the controller was able to extinguish the drift in the phase rapidly using only proportional control. The error in the phase between the two beams was reduced by factors 54 and 79 corresponding respectively to long fibers and original fibers. Comparing error reduction ratio for long fibers was necessary to assure modifications could be made to the current setup for application in future experiments. In the context of two-beam Raman transitions, the system can be used in future spin-orbit coupling experiments to ensure coherency.

VII. NOTES

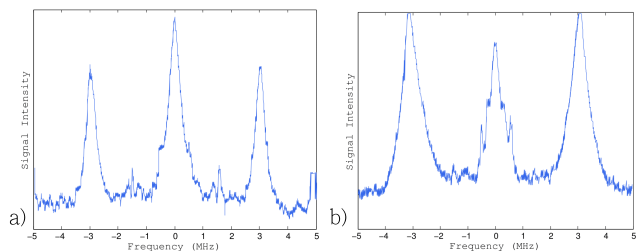### A. Interferometer Design Iterations

FIG. 14: Logarithmic signal intensity versus frequency measured at the photodiode for two different setup configurations — a) PBS cube overlap, b) coupling fiber.

The original design of the interferometer did not inclue optical fibers. Instead, another PBS cube was used to bring the two beams together, overlapping them onto the photodiode. Although we were able to attain a decent signal with this method, the current design discussed in III A was introduced to ensure accurate

beam overlap. The beat note reaching the photodiode in the current configuration is shown in fig. 14 b) alongside the old signal using the PBS cube. The setup containing the optical fibers shows a significant improvement in signal strength when we consider the logarithmic scaling for the signal intensity.

Looking back at fig 2 we see two boxes labeled "Amplifiers". These are actually RF sources and were used as such in our original design. In our current design we use a 80 MHz signal generator and a 83 MHz function generator as RF sources and use these other devices solely for their amplifiers — the actual RF source in the boxes were bypassed and the new source was connected straight to the amplifier. This alteration allowed us the ability to sync the signals to the same timebase. The importance of this was discussed in section III B.

B. Spectrum Analyzer Readings

While setting up the interferometer it is valuable to check that we were receiving the correct signal in the correct place. We can use a spectrum analyzer to visualize the signal intensity at all frequencies. The (logarithmic) signal intensity versus frequency figures that comprise this paper were attained from a HP 85623 Spectrum Analyzer with no digital output. To overcome this, we took photos of the spectra and used a boundary recognition code written in MATLAB in order to get a decent representation of the signals. This technique introduces a small amount of error in how the signals are pictured.

[1] V. Galitski, I.B. Spielman, "Spin-orbit coupling in quantum gasses", Nature, 494:49-54 (2013) 1

[2] Y.-J. Lin, K. Jiménez-García, I.B. Spielman, "Spinorbit coupled BoseEinstein condensates", Nature, 471:83-86 (2011)

[3] D. Jervis, J.H. Thywissen, "Making an ultracold gas", arXiv:1401.7659 (2014) 1

[4] D.J. Griffiths, *An Introduction to Quantum Mechanics*, 2nd Edition, Pearson Prentice Hall, 2005 2

1, 2